Erschienen in: Progress in Photovoltaics : Research and Applications ; 14 (2006), 6. - S. 513-531
https://dx.doi.org/10.1002/pip.690

Chemical Natures and Distributions of Metal Impurities in Multicrystalline Silicon Materials

T. Buonassisi[1], A. A. Istratov[1*,†], M. D. Pickett[1], M. Heuer[1], J. P. Kalejs[2], G. Hahn[3], M. A. Marcus[4], B. Lai[5], Z. Cai[5], S. M. Heald[6], T. F. Ciszek[7], R. F. Clark[8], D. W. Cunningham[8], A. M. Gabor[9], R. Jonczyk[10], S. Narayanan[8], E. Sauar[11] and E. R. Weber[1]

[1]*Department of Materials Science and Engineering, University of California, Berkeley, and Materials Science Division, Lawrence Berkeley National Laboratory, Berkeley, CA 94720, USA*
[2]*RWE Schott Solar, 4 Suburban Park Drive, Billerica, MA 01821, USA; Presently at: JPK Consulting, 54 Northgate Road, Wellesley, MA 02481, USA*
[3]*University of Konstanz, Department of Physics, 78457 Konstanz, Germany*
[4]*Advanced Light Source, Lawrence Berkeley National Laboratory, Berkeley, CA 94720, USA*
[5]*Advanced Photon Source, Argonne National Laboratory, Argonne, IL 60439, USA*
[6]*Pacific Northwest National Laboratory, Richland, WA 99352, USA*
[7]*Formerly: National Renewable Energy Laboratory, Golden, CO, USA/Presently: Siliconsultant, P.O. Box 1453, Evergreen, CO 80437, USA*
[8]*BP Solar, 630 Solarex Court, Frederick, MD 21703, USA*
[9]*Evergreen Solar, Inc., 259 Cedar Hill St., Marlboro, MA 01752, USA*
[10]*GE Energy, 231 Lake Drive, Newark, DE 19702, USA*
[11]*ScanWafer AS, PO Box 280, N-1323 Høvik, Norway*

We present a comprehensive summary of our observations of metal-rich particles in multicrystalline silicon (mc-Si) solar cell materials from multiple vendors, including directionally-solidified ingot-grown, sheet, and ribbon, as well as multicrystalline float zone materials contaminated during growth. In each material, the elemental nature, chemical states, and distributions of metal-rich particles are assessed by synchrotron-based analytical x-ray microprobe techniques. Certain universal physical principles appear to govern the behavior of metals in nearly all materials: (a) Two types of metal-rich particles can be observed (metal silicide nanoprecipitates and metal-rich inclusions up to tens of microns in size, frequently oxidized), (b) spatial distributions of individual elements strongly depend on their solubility and diffusivity, and (c) strong interactions exist between metals and certain types of structural defects. Differences in the distribution and elemental nature of metal contamination between different mc-Si materials can largely be explained by variations in crystal growth parameters, structural defect types, and contamination sources.

* Correspondence to: Andrei Istratov, Lawrence Berkeley National Laboratory, 1 Cyclotron Rd., Building 62-109 (MS 62R0203), Berkeley, CA 94720, USA.
[†]E-mail: istratov@berkeley.edu

KEY WORDS: multicrystalline silicon solar cells; transition metal impurities; contamination; crystal growth; synchrotron-based analytical X-ray microprobe techniques

Konstanzer Online-Publikations-System (KOPS)
URL: http://nbn-resolving.de/urn:nbn:de:bsz:352-2-6bi8a8mbc80y9

1. INTRODUCTION

Metals are known to exist in commercial multicrystalline silicon (mc-Si) materials in concentrations as high as 10^{14}–10^{16} cm^{-3} (Figure 1).[1–3] These impurities can decrease the efficiencies of silicon-based devices in a variety of ways, including bulk recombination,[4,5] increased leakage current,[6–8] and direct shunting.[9,10] The groundbreaking study of Davis *et al.*[11] specified threshold concentrations for individual metal species in Czochralski silicon (CZ-Si) photovoltaic devices, correlating the total metal content in a CZ-Si wafer to a quantified decrease in solar cell efficiency.

As newer multicrystalline silicon material evolved, the quantified effect of different metal species on device performance was found to vary from earlier studies.[12,13] It has become clear that in order to fully assess the effect of metals on solar cell performance, one must know not only the total concentrations of different metal species, but also about the spatial and size distributions of metal-related defects,[14–16] their chemical natures,[15–17] their interactions with different types of defects,[18–21] and their behavior[22,23] during the crystal growth process. In this study, we employ synchrotron-based analytical techniques to determine the aforementioned characteristics of metal contamination in a variety of mc-Si materials from multiple vendors. The conclusions drawn in this study are based on a large database of experimental data, which is much wider than a few typical metal distribution maps included in this article by way of example.

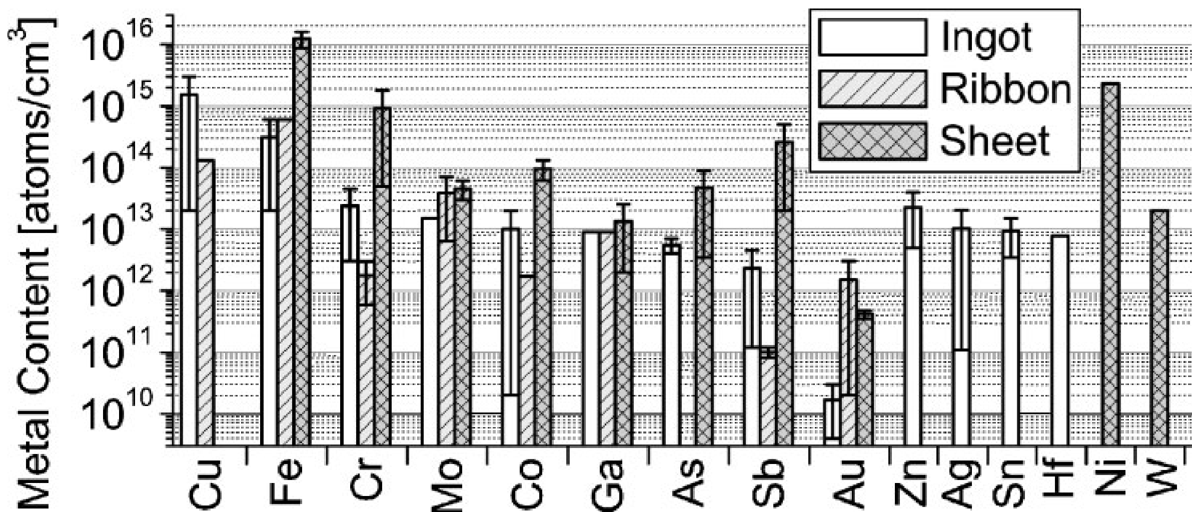

Figure 1. Neutron activation analysis data of total metal content in ingot-grown, ribbon, and sheet mc-Si materials, as determined from published data (references 1–3). NB: Total metal content is a strong function of feedstock quality, which can vary between growth runs. NB2: Since data was compiled from three different studies, sensitivity limits for one element may vary between materials. Thus missing bars for certain materials and elements do not indicate the absence of that metal in a particular material, simply a signal below a variable[87] detection limit

2. MATERIALS AND METHODS

2.1. Materials

The mc-Si materials analyzed in this study are directionally-solidified ingot-grown,[24] sheet,[25] and ribbon[26,27] materials originating from a variety of vendors, and multicrystalline float zone[28] grown at the National Renewable Energy Laboratory. While comprehensive information about these crystal growth techniques, throughput, and crystal growth parameters can be found in the references hitherto and in a review by T. F. Ciszek,[29] a brief summary is presented here to highlight the most relevant points for this study.

2.1.1. Directionally-solidified ingot-grown Mc-Si

This includes Bridgman, casting, and heat exchange method growth techniques,[24,29] which currently account for about 50% of the worldwide PV market.[30] A silicon ingot of a few hundred kg in mass is grown relatively slowly ($\sim$10 μm/s) from the bottom up within a crucible. Heaters control the cooling profile to ensure directional heat flow and to avoid the generation of secondary nucleation sites for crystallization. After cooling the ingot to room temperature during several tens of hours, the ingot is sliced into 'bricks' (vertical columns), which are then wire-sawed into wafers 250 μm thick or less.

We have examined and compared ingot-grown mc-Si material from three manufacturers, which will be distinguished as 'material A,' 'material B,' and 'material C.' Since variations in impurity distributions are known to exist along the height, i.e., along the growth direction, of the ingot,[3,31,32] samples from material A were extracted from three locations along the growth direction (bottom, middle, and top) of several ingots subject to different growth conditions, as well as near the edge of the ingot. Samples from the bottom of the ingot were analyzed for material B, as well as samples from near the top of the ingot from material C.

In contrast to the directional solidification growth methods of ingots, so-called 'ribbon' or 'sheet' growth techniques produce silicon wafers directly from the melt, thus eliminating the material loss incurred by wire sawing. A plethora of such growth techniques exists,[29,33] with different crucibles, growth substrates, and crystal pulling mechanisms. To distinguish between these different growth techniques, this study will adopt the following set of definitions:

2.1.2. Ribbon material

In this approach, a ribbon (i.e., a closed shape crystal in a sheet geometry) is pulled vertically from a melt with the growth interface remaining approximately perpendicular to the pull direction. The ribbon interface region is either confined in a meniscus defined by a die, which also gives the crystal its shape, or the meniscus may be formed directly from the bulk melt, as in CZ crystal growth. Crystal growth occurs without the support of a substrate. Following existing conventions, we refer to this material within the text as *ribbon mc-Si*. Examples of this type of ribbon material include *Edge-defined Film-fed Growth* (EFG)[26] and *String Ribbon* (SR).[34] Two types of ribbon materials were analyzed in this study.

2.1.3. Sheet material

In these growth techniques, a silicon melt in contact with a moving substrate is solidified as the substrate is pulled away from the hot zone of the furnace. Upon cooling, the solidified silicon detaches from the substrate either through the action of a release agent or a stress differential between the silicon crystal and the substrate. Sheet growth with the help of a substrate has the advantage that the crystal pull rate (determined by the velocity of the substrate) is essentially decoupled from the crystal growth velocity (which is nearly perpendicular to the substrate motion), in principle allowing for extremely high throughputs.[29,35] In the text, we refer to this mc-Si material as *sheet mc-Si*. Examples of materials defined as *sheet mc-Si* herein include *ribbon growth on substrate* (RGS)[24,27] and *SiliconFilm*.[36,37] Two types of sheet materials were analyzed, one using high-purity feedstock (Sheet A) and another using low-purity feedstock (Sheet B). The sheet material represented in Figure 1 also used a batch of lower-purity feedstock; cleaner feedstock comparable to that of aforementioned 'ribbon' materials would likely result in total metal contents similar to ribbon.

2.1.4. Multicrystalline float zone
Multicrystalline float zone (mc-FZ)[28] samples grown from melts intentionally doped with copper, iron, and titanium were also analyzed. While not commercial solar cell material, mc-FZ allows one to study the distribution, chemical nature, and effect on diffusion length of one impurity species at a time, making it a powerful research tool.

2.2. Analytical Methods

In this study, the principal analysis methods use an ultra-bright X-ray beam (10^{8-12} photons/s) produced by a synchrotron and focused down to a spot size between 200 nm and 5 μm in diameter, providing the high flux density necessary to detect and characterize nanometer-sized precipitates buried tens of microns below the surface (i.e., within the active device region of the solar cell). With this microfocused X-ray beam, one can perform a variety of experimental techniques.[38]

X-ray fluorescence microscopy (μ-XRF) is used to locate metal-rich particles and to determine their spatial distribution, elemental composition, and dimensions. The X-ray beam is maintained at a fixed energy, while the sample is scanned before the beam with an X-Y stage. At each step of the X-Y stage, an X-ray detector obtains information about which elements are present, via the characteristic fluorescence peaks. By plotting the magnitude of a given fluorescence peak at each point on the sample, a 2D map of the impurity distribution can be generated. While the sensitivity of the μ-XRF system is dependent upon many factors, including X-ray flux, spot size, and sensitivity of the detector, precipitates as small as 23 ± 5 nm in radius have been reported for optimized experimental conditions.[15] More details about the operational principles and detection limits of the μ-XRF technique can be found elsewhere.[15,38–40]

Once a metal precipitate is located, its chemical state can be determined via X-ray absorption microspectroscopy (μ-XAS). The position of the X-ray beam is fixed on the precipitate while the energy of the incoming X-ray beam is scanned in steps of 1 eV or less across the absorption energy edge of the impurity species of interest (e.g., Fe, Ni, Cu, etc.). An absorption spectrum results, which is unique for each chemical state of a given element. For example, different iron μ-XAS spectra will be obtained on iron silicide and iron oxide. Via comparison with standard materials, one can very accurately determine the chemical state of a given impurity species.[15,17,39]

The X-ray beam induced current (XBIC) is used to measure the recombination activity of defects in a method analogous to laser/light beam induced current (LBIC). The incoming X-ray beam is used to generate electron-hole pairs, which are then collected by a Schottky diode[41] or a pn junction.[9] XBIC can be used to determine the recombination activities of individual precipitates[16,40] and their impact on minority carrier diffusion length,[42] as well as to map larger sample areas by undersampling.[15]

By combining these three techniques (XBIC, μ-XRF, μ-XAS) at the same synchrotron beamline, the recombination activity, spatial distribution, size, elemental composition and chemical state of metal-rich particles in mc-Si materials can be obtained with a micron or sub-micron spatial resolution. The synchrotron beamlines utilized in this study include beamlines 2-ID-D[43,44] and 20-ID-B[45] of the Advanced Photon Source of Argonne National Laboratory, and beamlines 10·3·1[46] and 10·3·2[47] of the Advanced Light Source of Lawrence Berkeley National Laboratory.

3. RESULTS

The most characteristic observations for each type of material are shown in Table I, and can be summarized as follows (further details are provided in the subsequent sections):

3.1.1. Directionally-solidified ingot-grown material
Nanoprecipitates (diameter ≤ 200 nm), typically consisting of silicides of faster-diffusing metal species (e.g., Cu, Ni, Co, and/or Fe), are detected along certain grain boundaries (Figure 2), and are sometimes elongated along the grain boundary directions (Figure 3, particle #5). Such precipitates are predominantly found in the

Table I. Summary of observed particles in mc-Si materials. Not included in this table are metals homogeneously distributed along structural defects and metal point defects, most of which are below the detection limits of μ-XRF

Material \ Defect	Metal silicide nanoprecipitates	Metal-rich inclusions and microdefects
Directionally-solidified, ingot-grown mc-Si	Predominantly found near bottom, top, and edges of ingot along structural defects. μ-XRF at nanoprecipitates reveals Cu, Ni, Co, and/or Fe. Compared to other mc-Si materials, the slow cooling rate results in comparatively large (dia. > 30 nm) precipitates in comparatively low spatial densities along certain types of grain boundaries (Figure 7).	Predominantly found near bottom, top, and edges of ingot. μ-XRF at inclusions observes Ca, Cr, Fe, Mn, Mo, Ti, Zn, and/or traces of fast diffusers (Cu, Ni, Co). Microdefects (reported in references 10, 82, 83) can contain C, N, Fe, Cu, Ca.
Ribbon material (vertically-grown, without substrate)	Generally below detection limits of medium-sensitivity μ-XRF beamlines. Comparatively fast cooling rate likely responsible for smaller precipitates in higher spatial densities.	Unstable growth from melts with high impurity contents can result in a variety of inclusions and microdefects (reported in references 23, 84). None observed in high-purity materials analyzed in this study.
Sheet material (horizontal substrate-assisted growth)	Predominantly found along structural defects. μ-XRF detects Cu and Fe. Fast cool likely responsible for high spatial densities of small precipitates (Figure 7), sometimes below detection limit in samples with low impurity content.	μ-XRF detects intragranular inclusions in material with high impurity content, including Fe, Cr, Ni. Microdefects (reported in references 35, 85) can contain C, O.

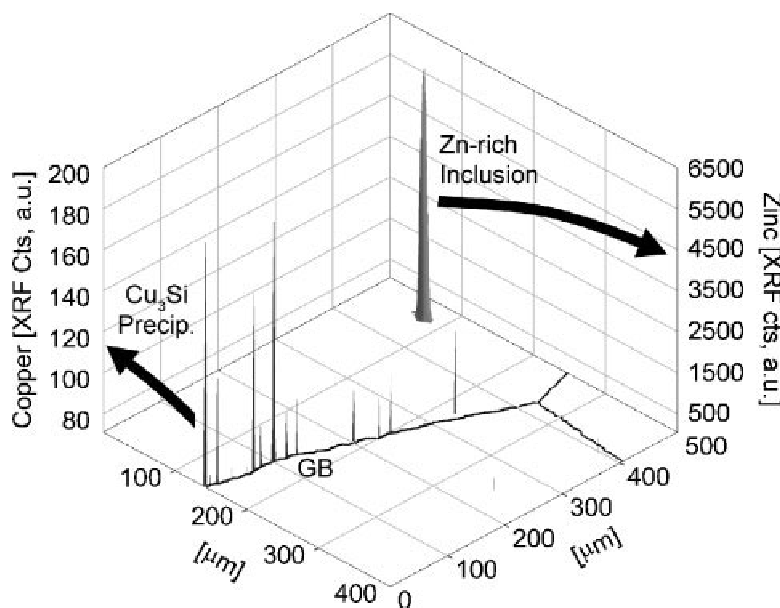

Figure 2. μ-XRF maps of Cu and Zn distributions in ingot-grown mc-Si, exemplifying the two types of metal-rich particle commonly observed in mc-Si: metal silicide nanoprecipitates (along a grain boundary, denoted by 'GB') and spatially-isolated inclusions up to several microns in diameter

bottom, top, and side (edge) regions of the ingot, and less frequently in the middle. Near the top of the ingot, smaller, more homogeneously distributed precipitates are observed.

Metal particles several microns in diameter, typically in an oxidized chemical state, are found in variable but much lower spatial densities. These particles are frequently found within the grains and toward the edges of

Copyright © 2006 John Wiley & Sons, Ltd.

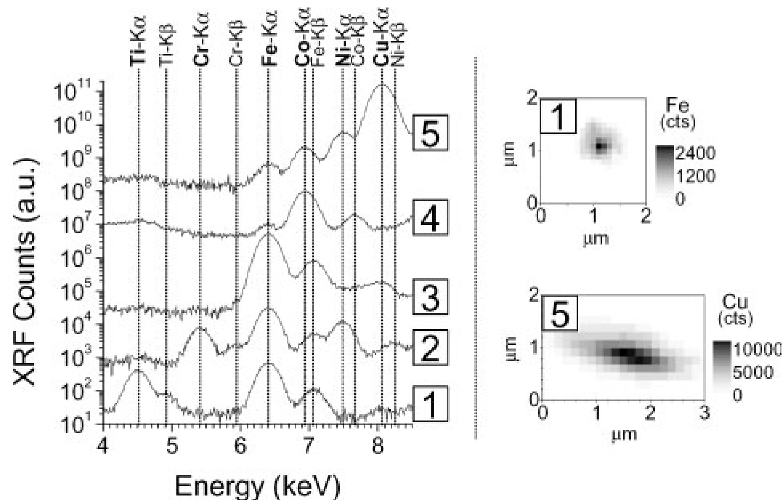

Figure 3. μ-XRF point spectra on impurity-rich particles in ingot-grown mc-Si material reveal a wide range of compositions and suggest a diversity of contamination sources. Two-dimensional μ-XRF maps reveal that particles of slower-diffusing species (e.g., '1,' top right) are often found within the grains, while particles of faster-diffusing species (e.g., '5,' bottom right) are often found at grain boundaries, sometimes elongated along the grain boundary direction

the ingot, and occasionally at grain boundaries (Figure 2). Their compositions can vary substantially (see Figure 3) but often include Fe and Ti, less frequently other elements such as Ca, Cr, Mn, Mo, and Zn, and sometimes additions of faster diffusers (Cu, Ni, and Co). More information about these particles can be found in Section 4·1.

3.1.2. Ribbon material

Multicrystalline silicon ribbon materials vertically grown by nonsubstrate-assisted methods were analyzed on beamlines of medium sensitivity (ALS 10·3·1 and 10·3·2). While these beamlines could detect metal-rich particles in most other as-grown mc-Si materials, no metal-rich particles were detected in the ribbon materials analyzed in this study, despite total metal contents comparable[2] to ingot-grown mc-Si. This suggests that metals in these ribbon materials are distributed more homogeneously and in smaller particles and point defects, below the detection limits of those beamlines. Higher-resolution beamlines, which have better sensitivities,[15] are necessary for the detection of these smaller particles.

3.1.3. Sheet material

Sheet materials horizontally grown by substrate-assisted methods were analyzed using high- (APS 2-ID-D and 20-ID-B) and medium-sensitivity (ALS 10·3·1 and 10·3·2) beamlines. In sheet material grown with high-purity feedstock (sheet material A), no metal-rich particles were detected in as-grown material, in agreement with the results from ribbon materials. As-grown material subjected to a post-growth anneal at high temperature, which allows existing precipitates to grow by absorbing metals in solution within the crystal, exhibited iron and copper particles along structural defects.

Within the grains and occasionally at grain boundaries in sheet material grown from low-purity feedstock (sheet material B), one observes a low density of clusters, tens of microns across, containing micron-sized particles consisting of iron silicide, nickel silicide, and chromium silicide. Rarely, oxidized particles up to 25 μm diameter can be observed. More information about these particles can be found in reference 15. In as-grown material subject to a 800°C anneal for 4 h, iron silicide nanoprecipitates can be observed in high densities along grain boundaries and intragranular defects, believed to be voids[36] or another type of micro-defect. Were all the iron silicide precipitated at grain boundaries and at intragranular defects to be dissolved

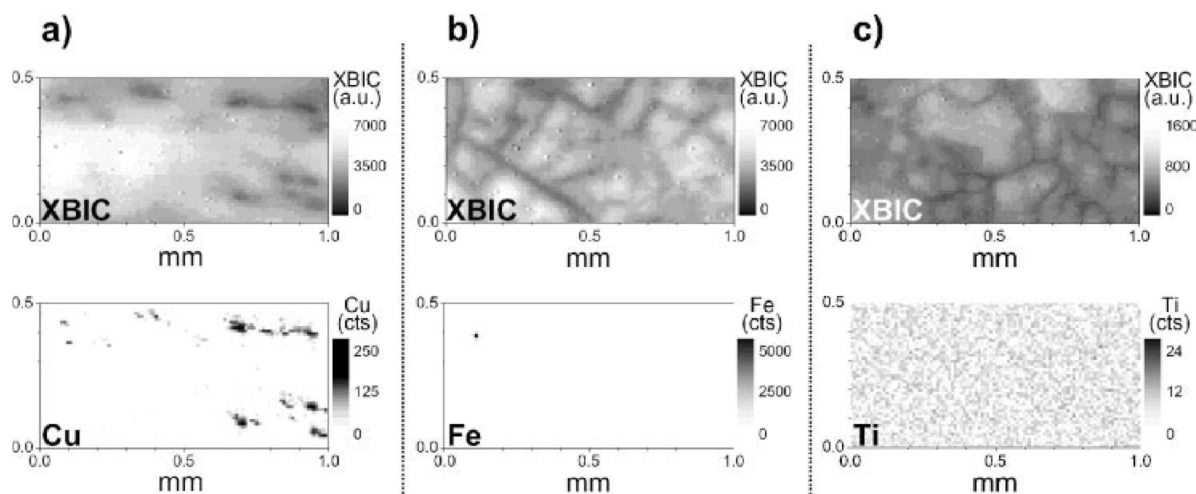

Figure 4. XBIC (above) and μ-XRF (below) maps of multicrystalline float zone silicon grown from metal-doped melts of (a) copper, (b) iron, and (c) titanium. Whereas high-flux Cu tends to form relatively isolated metal-rich particles or clusters of particles, low-flux Ti and Fe tend to form metal point defects and homogeneously coat structural defects (as evident in XBIC), often below the current detection limits of the μ-XRF technique. Occasionally, large inclusions can be detected (e.g., Fe)

homogeneously throughout the sample, estimates indicate that bulk concentrations up to 10^{15} Fe/cm^3 could be reached.[15]

3.1.4. Mc-FZ doped with copper

Mc-FZ containing (3–4) $\times 10^{16}$ cm^{-3} Cu (arising by intentional melt doping during growth) demonstrate large, recombination-active Cu_3Si particles (or clusters of particles) along structural defects such as grain boundaries and dislocations (Figure 4a). The distribution of copper at structural defects is inhomogeneous, in agreement with previous studies,[48–50] such that the spaces between precipitates exhibit noticeably lower recombination activity.

3.1.5. Mc-FZ doped with Iron

In mc-FZ containing approximately 10^{16} cm^{-3} Fe (by intentional melt doping during growth) a few micron-sized iron silicide particles are detected in low spatial densities (e.g., Figure 4b). While these Fe silicide particles coincide with a locally decreased XBIC, the predominant features observed in XBIC maps are highly recombination-active grain boundaries and intragranular regions. These are present to a much lesser extent in undoped reference mc-FZ material, indicating that a high density of nm-sized defects (precipitates and metal point defects) are present with dimensions below the detection limits of the experimental conditions used in this study. The large $FeSi_2$ particles observed in the μ-XRF scans are probably incorporated into the material as inclusions directly from high iron concentrations in the boundary layer of the interface melt.

3.1.6. Mc-FZ doped with Titanium

Mc-FZ containing 5×10^{13} cm^{-3} Ti (by intentional melt doping during growth) exhibited no Ti-rich particles above the μ-XRF detection limits chosen for this study (Figure 4c, noise only is visible). Nevertheless, structural defects and intragranular regions demonstrated exceptionally high recombination activities, suggesting a fine distribution of metal atoms or particles below the detection limits of the experimental conditions used in this study. Impurity segregation to structural defects during crystal growth, which may be responsible for the recombination activity of structural defects in this sample, will be discussed in Section 4 2.

4. SIMILARITIES OF METAL CONTAMINATION BETWEEN MC-SI MATERIALS

4.1. Two classes of metal-rich particles

The metal-rich particles in all materials analyzed herein can be divided into two distinct classes: (a) the metal silicide (e.g., $FeSi_2$, $NiSi_2$, Cu_3Si, etc.) nanoprecipitate, typically up to several tens of nanometers in diameter, most often associated with structural defects, and (b) the occasional larger particle, up to several microns in diameter, which is frequently oxidized, found within the grains, and/or composed of multiple slowly-diffusing metal species reminiscent of foreign material inclusions (e.g., coming from stainless steels, furnace material, etc.). These two distinct classes of metal-rich particle are shown in Figure 2, which portrays a representative μ-XRF map of an ingot-grown mc-Si sample from near the top of an ingot.

Metal silicide nanoprecipitates are the more frequently observed type of metal-rich particle and are likely to have formed from metals incorporated in the crystal in solid solution. Although most classes of metal silicide compounds can be synthesized in the laboratory (e.g., Fe_3Si, FeSi, $FeSi_2$), only the most silicon-rich metal silicides (e.g., $FeSi_2$, Cu_3Si, $NiSi_2$, etc.) are observed in mc-Si materials. This observation is consistent with the assumption that these precipitates are formed in a silicon-rich environment through precipitation of initially-dissolved metal atoms. Metals can enter into the mc-Si crystal via the melt, from the growth surfaces, or by dissolving from larger particles (e.g., inclusions) within the crystal during cool-down. For more information about the contamination pathways of metals into mc-Si, the reader is referred to reference 15.

Metal-rich particles over 1 μm in size, especially those containing oxidized and/or slowly-diffusing species, are believed to be incorporated directly from the melt during crystal growth. Examples include the 12 μm diameter ZnS particle in Figure 2, and the oxidized iron particles previously reported by McHugo *et al.*[17,51] Most oxidized metal compounds are not expected to form under equilibrium conditions within silicon,[16] and several of these particles are too large to be explained by the precipitation of supersaturated impurities during cooling. These facts, plus the compositions of these particles, indicate that these are inclusions, i.e., incompletely-dissolved foreign particles introduced into the melt and engulfed by the advancing solidification front during crystallization. For more information about these particles, see reference 15.

4.2. Metal—structural defect interactions

In almost all materials analyzed in this study, metal silicide precipitates are detected at structural defects, especially two-dimensional defect surfaces such as grain boundaries and voids, in agreement with previous studies.[23,52–54]

The appearance of metal-rich particles at structural defects is likely due to a combination of processes. Firstly, impurity atoms in solution (i.e., dissolved) in the crystal at high temperatures supersaturate upon cooling, and then seek the most energetically favorable sites[55] for second-phase (e.g., metal silicide) precipitate nucleation. Precipitates are most often detected by μ-XRF at regions of greatest strain or lattice deformities as a consequence of the lower nucleation barrier for precipitation in those regions. Secondly, impurity atoms such as iron[56] and copper[57] have been observed to segregate to structural defects even at elevated temperatures; upon cooling, these metals will form precipitates when they reach a supersaturated state. Thirdly, if metals are present in locally high concentrations in the melt, they can precipitate directly from the melt at structural defects that perturb the solidification front, for example grain boundaries, when a locally high metal content exists at the liquid solid interface.[23,54] Such perturbations of the solidification front are also believed to favor the incorporation of foreign particles (e.g., oxidized Ti or Fe) in the melt as inclusions.[58] The end result of all these processes is the accumulation of metals at structural defects in mc-Si; additional discussion can be found in reference 15.

The capacity of a given type of structural defect to absorb transition metals is a parameter that is known to vary in a somewhat predictable manner.[19,20,56,57] Since different mc-Si materials tend to have unique sets of structural defect types, one may expect variations in the amount of transition metal precipitation at structural defects from one material to another. This point is further discussed in Section 5·2.

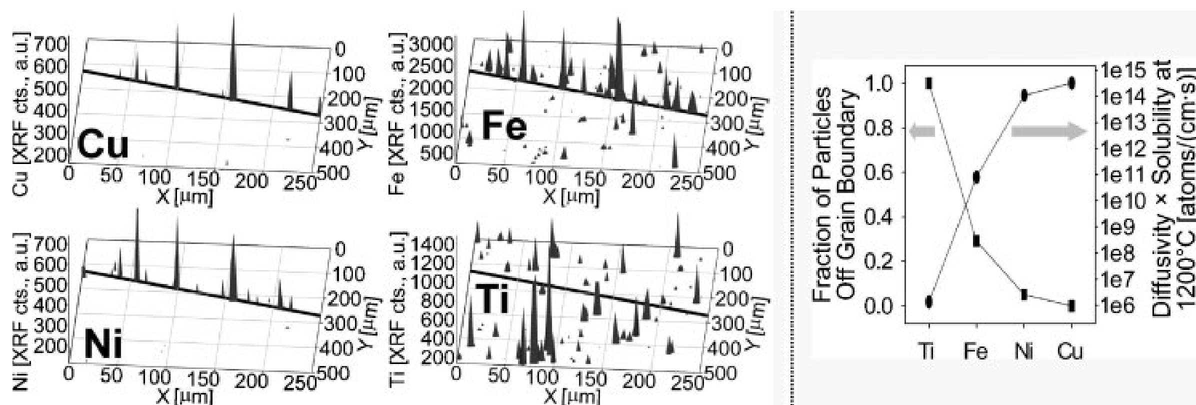

Figure 5. Dependence of elemental distribution in ingot-grown mc-Si on diffusivity and solubility. The four μ-XRF maps to the left depict a grain boundary (shown as a thick line) in material extracted from near the edge of an ingot, and surrounding intragranular regions. Particles of low-flux species (e.g., Ti) are often found within the grains, while particles of high-flux species (e.g., Cu, Ni) are often found aggregated in a fewer total number of particles, usually at structural defects such as grain boundaries

4.3. Element-specific spatial distributions

Some elements tend to aggregate in nanoprecipitates along grain boundaries, while others are found predominantly in large intragranular particles, as evident in Figure 5. This divergence can be partially explained by element-specific fluxes and degrees of supersaturation in the material. The product of the solubility [atoms/ cm^3] and diffusivity [cm^2/s] of an elemental species at a temperature T yields its *atomic flux* $[(atoms/cm^3 \cdot s) \cdot cm^2]$, which describes impurity transport within the crystal. Once the total concentration of a given impurity species exceeds its solubility at a given temperature, a driving force for precipitation develops, and the atomic flux determines the distance a certain fraction of impurity atoms can travel before precipitating or forming point defects. In addition, differences in elemental impurity distributions are partly explained by the way different elements are present in the melt and introduced into the crystal (atomically dissolved metals vs. foreign particles of Ti- or Fe-oxide containing many millions of atoms).

Elements with higher atomic fluxes (e.g., Cu and Ni) are predominantly found in silicide nanoprecipitates (10's or 100's of nm in diameter) at grain boundaries or other structural defects, as shown in Figure 5. Their more gradual temperature dependences of solubility combined with high diffusivity allow them to diffuse to the most stable sinks (e.g., grain boundaries), where nucleation barriers for precipitation are lower. Precipitates of these elements are typically the easiest to detect by μ-XRF, reflecting both their higher solubilities as well as their tendency to be concentrated at select locations with relatively large distances between particles. This reduces the concentration of dissolved metals and smaller precipitates elsewhere and improves material performance between particles (e.g., Figure 4a).

Elements with medium (e.g., Fe) or low (e.g., Ti) atomic fluxes are more frequently found in intragranular defect particles, as Figures 2 and 5 demonstrate. These atoms are less likely to dissolve from inclusions formed during crystal growth, and thus are less likely to diffuse to structural defects and form precipitates. On the other hand, metals in solution with low atomic fluxes cannot diffuse very far during cooling and tend to precipitate locally upon supersaturating, forming precipitates that are much smaller and closer-spaced than those of metals with higher atomic fluxes, as deduced from Figures 4b and 4c. Unfortunately, point defects of these low-flux species are known to form deep levels in the silicon bandgap.[59,60] Thus, it is not surprising that elements of lower atomic fluxes tend to be more harmful for solar cell device performance,[11,18,59] since these elements form closer-spaced and more recombination-active defect centers.

Elemental distributions in the solidified mc-Si material also depend on the way elements are introduced into the crystal. μ-XRF and μ-XAS measurements show Fe and Ti often contained in oxidized particles containing up to 10^8–10^{15} atoms, which are likely inclusions of foreign particles. These compounds have high melting temperatures ($T_M[Fe_2O_3] = 1565°C$; $T_M[TiO_x] > 1700°C$) and will likely survive for a limited time in the

silicon melt, especially if the melt already contains high concentrations of the dissolved impurity. Once incorporated into the crystal, the low fluxes of these metals and high binding energy to oxidized compounds hinders metal dissolution from inclusions into the grains. On the other hand, copper oxides have melting temperatures below that of silicon, so these particles likely dissolve in the melt prior to their incorporation into the mc-Si crystal, facilitating silicide precipitate formation during cool-down.

5. *DIFFERENCES IN METAL CONTAMINATION BETWEEN MC-SI MATERIALS*

5.1. Contamination sources

Impurities may enter the mc-Si crystal from any nonsilicon object, whether from feedstock or crystal growth, which is directly or indirectly in contact with the melt or cooling crystal. Impurities observed in mc-Si reflect a wide variety of different contamination sources, as shown in Figure 3. One contamination source is stainless steel, which both this and previous studies[15,61] have observed, likely originating from furnace parts, growth surfaces,[62] or feedstock. These and other studies[2] reveal the presence of other metals from furnace parts (Mo, Cu, Ti, and Mn) and metals possibly associated with materials coating growth surfaces[62] (e.g., Si_3N_4 sintering agents such as Fe[63] and Hf[64]). Metals may also diffuse from crucible walls directly into the mc-Si ingot after crystallization.[62,65–67] Impurity concentrations may vary from run to run in the same process equipment, or even from one region to another in the same crystal, for example along the height of an ingot or between different ingots.

Because different types and concentrations of metal impurities have varying effects on minority carrier diffusion length,[18] control over all process parameters and impurity sources (feedstock, growth surfaces, furnace parts, etc.) is necessary to ensure the production of mc-Si material of consistently reproducible quality.

5.2. Structural defects

A number of studies[19–21] indicate that each type of structural defect has its own capacity for transition metals, which affects the ability for the segregated metals to aggregate at the defect and eventually form precipitates during crystal cool-down. Evidence for this is shown in Figure 6, which compares grain boundary decoration in ribbon and in ingot-grown mc-Si samples. The grain boundary locations were determined by the intensity of the elastically scattered X-ray beam in the direction of the detector (a function of grain orientation). In the ingot-grown mc-Si sample, metal silicide precipitates are detected at some grain boundaries but not at others, while no metal-rich particles are detected in ribbon. While differences in grain boundary metal decoration between ingot and ribbon materials is also influenced by other factors (namely crystal cooling rates), local differences within the same material can be explained only by differences in structural defect character and density.

The crystal growth conditions play a large role in determining the densities and types of structural defects within the crystal,[68–70] i.e., the density of precipitation sites for impurities. Large-angle and random grain boundaries common to sheet[36,37] and ingot-grown mc-Si are the easiest for precipitate nucleation, given model defect studies.[19,20] This is supported by the greater abundance of metal nanoprecipitates detected by μ-XRF at these defect types (e.g., Figure 6). Such structural defects with large capacities for impurities will also act as internal gettering sites, reducing the metal point defect concentration[71] and increasing the minority carrier diffusion length within the grains. On the other hand, $\sum 3 < 111 >$ twin boundaries common to both ingot-grown mc-Si and ribbon[26,27,72] offer fewer segregation and nucleation sites for metals. Metal precipitates are seldom observed by μ-XRF at those locations in these materials.

Interactions between metals and structural defects can either be advantageous[73,74] or detrimental[18,28,75] for solar cell device performance, depending on the spatial density, location (especially with respect to the pn-junction), and character of structural defects within the device. If one could, during crystal growth, reliably control the types of structural defects and their densities, one would subsequently reduce the variability in the sizes and densities of metal silicide nanoprecipitates. This, in turn, would reduce the variability of the impact of metallic impurities on performance.

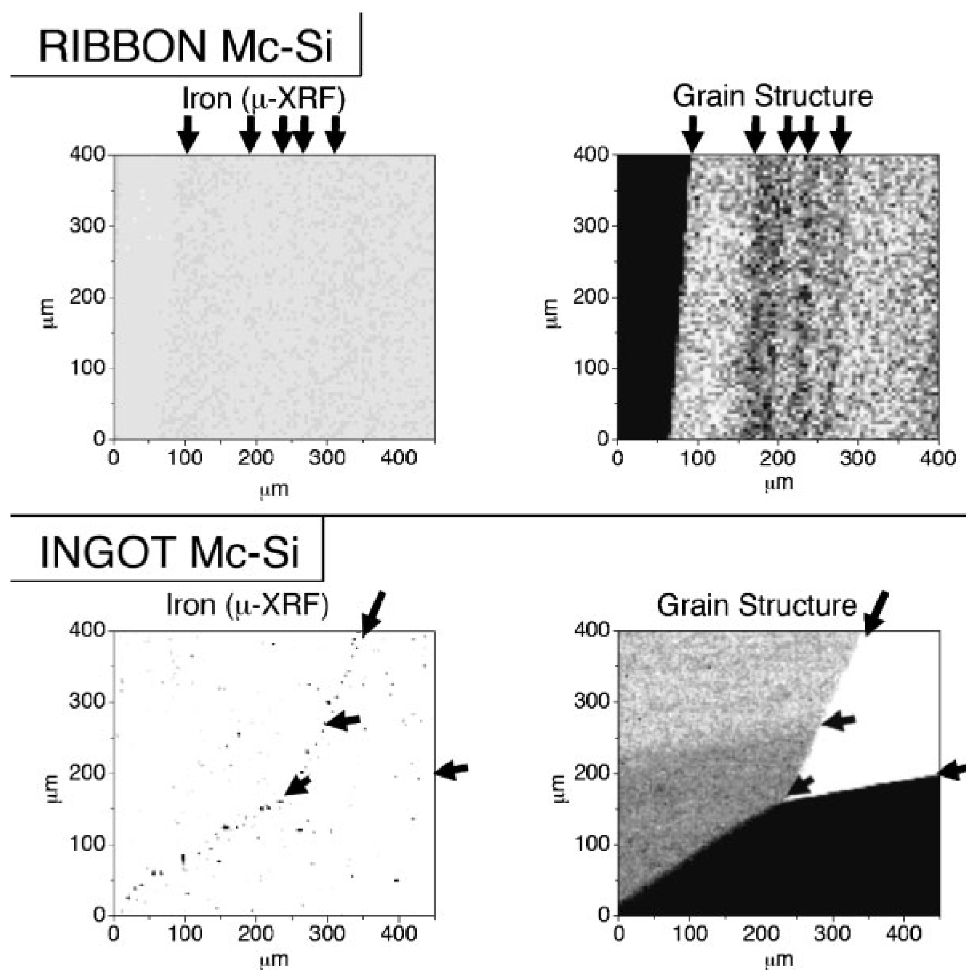

Figure 6. μ-XRF maps of iron distributions in ribbon and directionally-solidified mc-Si, using the elastically scattered X-ray beam peak intensity to determine grain structure. Metal silicide nanoprecipitates are detected along certain structural defects in the ingot-grown mc-Si, whereas in ribbon materials, no metal-rich particles are detected. This difference can stem from two possible (nonexclusive) phenomena: (a) the faster cooling rate of ribbon mc-Si and a low metal concentration favor the formation of smaller precipitates below the current detection limits of μ-XRF, and (b) the structural defects in ribbon (especially 60° twin boundaries) have less capacity for metals than the high-angle twin and random grain boundaries of ingot-grown mc-Si and sheet materials

5.3. Crystal growth variables

5.3.1. On the size and distribution of metal silicide nanoprecipitates

In addition to structural defect density discussed in the previous section, at least three other crystal growth variables combine to determine the size and spatial distribution of metal silicide nanoprecipitates: (1) the cooling rate during crystal growth, (2) the total metal content, and (3) variations of crystal growth conditions as growth progresses. Since it is necessary to decouple these effects to fully understand them, the next paragraphs describe examples where one or two of the variables are held constant, while a second and/or third is altered.

To study the effect of cooling rate on nanoprecipitate size and spatial distributions, one can select ribbon and ingot-grown mc-Si materials with comparable total metal contents,[2] but orders of magnitude different interface cooling rates (approximately 1000–2000°C/min for ribbon, 20–100°C/min for ingot-grown, according to reference 26). While metal silicide precipitates can be detected by μ-XRF along certain grain boundaries in the

ingot-grown mc-Si sample, ribbon material exhibits no such precipitates above the detection limits (Figure 6). This can be explained by the effect of cooling rate on the spatial and size distributions of metal precipitates. Assuming a fixed initial impurity content, faster cooling rates (>100°C/min.) during crystal growth result in faster impurity supersaturation, which in turn provides a stronger driving force for metals in solution to precipitate locally. Consequently, faster-cooled materials (e.g., ribbon and sheet) contain metal nanoprecipitates with relatively smaller average sizes and higher spatial densities.[76,77] On the other hand, slow cooling after growth (<20°C/min.), typical of ingot-grown mc-Si, allows impurity atoms to diffuse over much larger distances and accumulate preferentially at the most energetically favorable sites, resulting in a few large particles separated by larger distances.

The effect of total metal concentration on nanoprecipitate size is seen by comparing materials with dissimilar metal contents, but comparable cooling rates. Sheet material B experiences cooling rates comparable to ribbon materials and sheet material A, but contains one to two orders of magnitude greater metal content. As a consequence, metal silicide nanoprecipitates (∼46 nm diameter) are detected along structural defects in sheet material B (Figure 7), while no precipitates are above the detection limits in the other sheet and ribbon materials. A higher dissolved metal concentration in sheet material B is likely to provoke supersaturation—and thus the onset of precipitation—at a higher temperature, when the atomic flux of impurities is orders of magnitude larger, allowing impurities to accumulate at stable sinks such as grain boundaries.

Inevitably, variations of crystal growth conditions occur as crystal growth progresses. Hence, different regions of the ingot or in different wafers of ribbon or sheet mc-Si (depending on the time elapsed from the beginning of the growth run[26]) can be expected to have different concentrations and distributions of impurities. Independent studies have demonstrated how the total metal content[3] and the iron point defect concentration[31,32] vary as a function of ingot height, largely because of impurity segregation from the solid to the melt, in-diffusion of impurities from growth surfaces, and back-diffusion after solidification. We observe similar trends: near the middle of the ingot, where segregation has reached a steady-state and the dissolved metal concentration[31,32] and total metal content[3] are lower than near the culmination of growth at the top of the ingot, metal silicide nanoprecipitates are not readily detected. On the other hand, metal silicide nanoprecipitates are readily observed in three locations: (a) near the top of the ingot, due to impurity segregation during growth, (b) near the edges of the ingot, arising from impurity indiffusion from the growth surfaces, and (c) near the bottom of the ingot, arising from the latter effect concomitant with nonsteady-state segregation of impurities during the early stages of ingot growth.

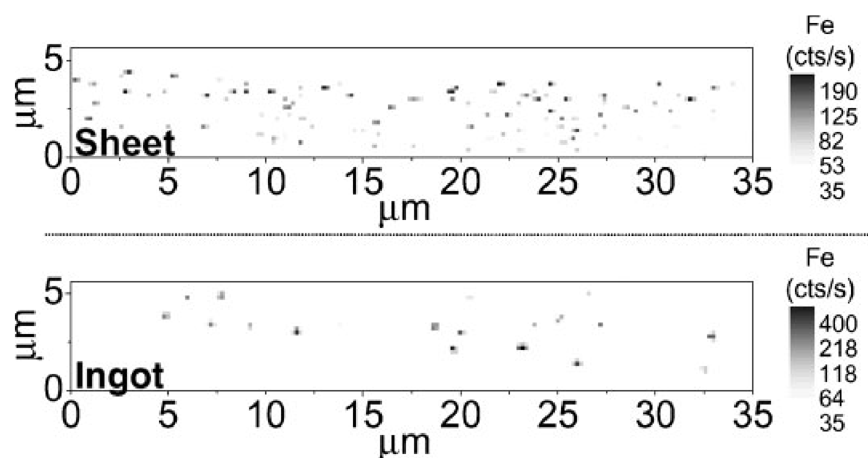

Figure 7. Comparison of size and spatial distribution of iron silicide nanoprecipitates in grain boundaries of sheet mc-Si grown with the aid of a substrate (above) and ingot-grown mc-Si (below) from near the bottom of the ingot. A lower density of larger (note the Fe count rate, right) nanoprecipitates is detected by µ-XRF in the ingot-grown mc-Si sample, likely a reflection of the slower cooling rate of ingot-grown mc-Si

5.3.2. On the size and distribution of inclusions

We have studied many tens of inclusions during our investigations, which lead us to conclude that inclusion size and distribution can be affected by two crystal growth variables: (a) crystal growth velocity (or 'crystal pull velocity'), and (b) stability of the growth process.

Under stable growth conditions, the growth velocity is one of the key parameters that determine the maximum size of second-phase particle incorporated by the advancing solidification front. Slower-moving solidification fronts tend to push large, second-phase particles in the melt forward like a snow-plow, while faster-moving solidification fronts increase the chances of these particles being incorporated as inclusions.[58] Our observations are consistent with this model: the largest single particle inclusion was observed in fast-solidified sheet Material B, as shown by the dotted horizontal line in Figure 8. On the other hand, the sizes of single particles in slowly-solidified ingot-grown mc-Si were comparatively smaller. It must be noted that the size and chemical state distributions of impurity-rich particles in the original contamination sources (e.g., growth surfaces, feedstock, growth environment) strongly influence the maximum inclusion size detected in as-grown mc-Si.

The largest and most abundant inclusions in both ingot-grown mc-Si and sheet material B are generally found in first or last regions of the crystal to solidify, or near the growth surfaces. In ingot-grown mc-Si, this corresponds to material near the edges of the crucible, as well as near the bottom and the top of the ingot. Incidentally, these regions are also where the majority of metal silicide precipitates are observed, suggesting that unstable crystal growth[22] and high metal concentrations dissolving from growth surfaces favor the formation of these nanodefects.

The presence of foreign particles in the melt can adversely affect mc-Si material performance. If metals are dissolved from foreign particles, this increases melt impurity levels and leads to a higher level of decoration of structural defects at the interface, also increasing the recombination activity[48,78–80] of those defects in the crystal. Foreign metal-rich particles incorporated directly into the material as inclusions affect only a small volume

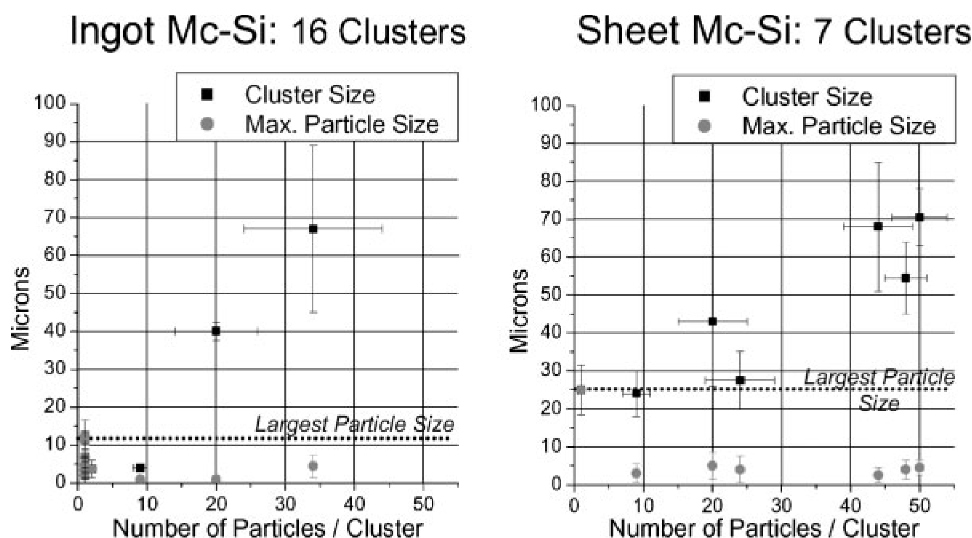

Figure 8. Size distributions of inclusion clusters and of the individual particles composing the clusters, detected by μ-XRF in ingot-grown (16 inclusion clusters analyzed) and sheet (7 clusters analyzed) mc-Si materials. Inclusions are often observed in regions of unstable crystal growth (e.g., near growth surfaces, and within the first and last regions of the crystal to solidify). Ingot-grown mc-Si has a predominance of single particle inclusions with comparably smaller maximum size, with the exception of two large inclusion clusters observed near the edge and bottom of an ingot. In sheet mc-Si, large clusters of particles are frequently observed, especially towards the backside (i.e., the last to solidify) of the material, as well as a comparatively large single particle. The different size distributions of clusters in the two materials are believed to stem from differences in crystal growth, such as the solidification velocity and feedstock quality

of material around the inclusion, provided these are not formed from a metal species with sufficiently high atomic flux to be liberated during subsequent solar cell device processing.[80,81]

6. CONCLUSIONS

Synchrotron-based analytical techniques were employed to systematically study and compare the distribution and nature of metal-rich particles in different mc-Si materials: sheet mc-Si from two manufacturers, ribbon mc-Si from two manufacturers, multicrystalline float zone intentionally doped with metals during crystal growth, and directionally-solidified mc-Si from three distinct manufacturers. Many similarities and differences regarding the size and spatial distributions, chemical and elemental natures, and abundances of metal-rich particles were observed in these materials. Similarities, such as the presence of two types of metal-rich particle (silicide nanoprecipitates and larger, sometimes oxidized inclusions), and the affinity for metals to precipitate at structural defects such as certain types of grain boundaries and intragranular defects, indicate some commonalities regarding contamination pathways and the physics governing metals in mc-Si.

Most of the differences observed between materials can be attributed to the crystal growth conditions and external contamination sources. Metals detected by μ-XRF can typically be traced back to specific parts of the production process (e.g., feedstock, material lining growth surfaces, etc.). The final distribution and form of metals, which most severely affects device performance, is dictated not only by the nature (i.e., diffusivity and solubility) of the contaminants, but also by a handful of crystal growth parameters: the crystal growth velocity, the total time silicon remains in a molten state, the character and density of structural defects, and most significantly, the cooling rate. Fast-cooled materials such as ribbon and sheet material tend to have larger densities of smaller precipitates, while more slowly-cooled material such as ingot-grown mc-Si and mc-FZ exhibit a comparatively lower density of larger metal silicide precipitates.

These differences underscore two important points: (1) the critical impurity content for one mc-Si material or processing sequence may not necessarily be the same for all others. Material-specific crystal growth conditions and contamination sources can produce differences in the spatial distribution and chemical nature of metals, which directly affects the minority carrier diffusion length and its response to processing. Thus, one must individually evaluate threshold values for impurity content and nature in the feedstock and production environment for each mc-Si material. (2) A complete material-specific optimization of solar cell device processing must take these differences into consideration.

Our observations on three types of mc-Si materials can be summarized as follows: Multicrystalline silicon ribbon material, because of the rapid cooling during growth which does not allow dissolved impurities to diffuse far before precipitating, the predominance of structural defects with comparatively lower capacity for impurities (e.g., 60° twin boundaries), and the low total transition metal concentration, reveals no metal precipitates above the detection limits of this study. We thus conclude that metals are distributed in a higher density of smaller precipitates and point defects, which could explain the lower performance of as-grown ribbon materials[86] relative to ingot-grown mc-Si. However, effective processing, especially phosphorus diffusion, H-passivation, and aluminum gettering can substantially increase performance.[27,86]

Sheet material appears to be similar to ribbon, but key differences include feedstock quality and structural defect density and character. In sheet mc-Si grown from feedstock containing high total metal concentrations, material performance can benefit from the proper amount and (three-dimensional) location of random, equiaxial grain boundaries, which serve as nucleation sites for transition metal precipitates, which in turn reduce the metal content[68] within the grains. Metals are also found concentrated in intragranular defects and, due to cleverly chosen growth conditions, segregated toward the back of the wafer[13] (away from the pn junction) during growth. Even with high total impurity contents, these mechanisms contribute to reduce the impacts of metals on device performance. The vast majority of these metals cannot be effectively removed during processing because of their high concentrations, so effective defect engineering of metals within the material is necessary in addition to optimized processing to ensure performance comparable to ingot-grown mc-Si.

Ingot-grown mc-Si in many respects represents the intersection of the two material types discussed above. Metal silicide nanoprecipitates of fast-diffusing species are observed along certain structural defects with high

capacities for impurities, but not along others. Those structural defects are effective internal gettering sites for metal point defects during the slow ingot cool, and the concentration of point defects can be reduced considerably. However, one must keep this initial defect distribution in mind when optimizing solar cell processing, as to avoid possible re-dissolution of metals from silicide nanoprecipitates back into the grains. Slower-diffusing impurities are frequently observed at intragranular inclusions, often in an oxidized chemical state and/or present with other metals that indicate the origins of contamination as the feedstock, crucible walls, and/or furnace parts. Although these particles themselves are in too low spatial density to significantly impact diffusion lengths, any metals dissolved from these inclusions during growth or subsequent processing can lead to decreased performance.

ABBREVIATIONS

Types of silicon solar cell materials

CZ-Si: Czochralski silicon
mc-Si: Multicrystalline silicon
mc-FZ: Multicrystalline float zone silicon

Characterization techniques

LBIC: Laser/light beam induced current
μ-XRF: X-ray fluorescence microscopy
μ-XAS: X-ray absorption microspectroscopy
XBIC: X-ray beam induced current

Synchrotron facilities

ALS: Advanced Light Source, at Lawrence Berkeley National Laboratory
APS: Advanced Photon Source, at Argonne National Laboratory

Less common elements

Hf: Hafnium
Mn: Manganese
Mo: Molybdenum

Acknowledgements

This study would not have been possible without the collaboration and assistance of numerous industrial partners, some of whom chose to remain anonymous. The authors also thank influential discussions with a variety of colleagues over the years that helped shape our current understanding: C. Ballif, O. Breitenstein, A. Cuevas, L. J. Geerligs, S. Glunz, U. Gösele, J. Isenberg, M. Kittler, D. Macdonald, S. Peters, J.-P. Rakotoniaina, S. Riepe, W. Schröter, M. Schubert, M. Seibt, W. Seifert, R. Sinton, H. Väinölä, O. F. Vyvenko, W. Warta, P. Zhang, A. Ziegler, among many others. S. Fakra is acknowledged for her assistance at Beamline 10.3.2. This study was supported by NREL subcontract AAT-2-31605-03, and impurity-doped float zone silicon crystal growth at NREL was supported by U.S. Department of Energy Contract No. DE-AC36-99GO10337. The operations of the Advanced Light Source at Lawrence Berkeley National Laboratory are supported by the Director, Office of Science, Office of Basic Energy Sciences, Materials Sciences Division, of the US Department of Energy under Contract No. DEAC03-76SF00098. Use of the Advanced Photon Source was supported by the US Department of Energy, Office of Science, Office of Basic Energy Sciences, under Contract No. W-31-109-ENG-38.

REFERENCES

1. Macdonald D, Cuevas A, Kinomura A, Nakano Y. Phosphorus gettering in multicrystalline silicon studied by neutron activation analysis. *Proceedings of the 29th IEEE Photovoltaic Specialists Conference*, New Orleans, USA, 2002; 1707–1710.
2. Istratov AA, Buonassisi T, McDonald RJ, Smith AR, Schindler R, Rand JA, Kalejs JP, Weber ER. Metal content of multicrystalline silicon for solar cells and its impact on minority carrier diffusion length. *Journal of Applied Physics* 2003; **94**: 6552–6559.
3. Macdonald D, Cuevas A, Kinomura A, Nakano Y, Geerligs LJ. Transition-metal profiles in a multicrystalline silicon ingot. *Journal of Applied Physics* 2005; **97**: 033523.
4. Istratov AA, Hieslmair H, Weber ER. Iron contamination in silicon technology. *Applied Physics A: Material Science & Processing* 2000; **70**: 489–534.
5. Istratov AA, Weber ER. Physics of copper in silicon. *Journal of the Electrochemical Society* 2002; **149**: G21–G30.
6. Lee K, Nussbaum A. The influences of traps on the generation-recombination current in silicon diodes. *Solid-State Electronics* 1980; **23**: 655–660.
7. Simeonov SS, Ivanovich MD. Recombination current in abrupt semiconductor p-n junctions. *Physica Status Solidi (a)* 1984; **82**: 275–284.
8. Morita M, Muramatsu Y, Watanabe K, Nishio N, Taketomi T, Shimono T. In *Diagnostic techniques for semiconductor materials and devices; Vol. 92–2*, Rai-Choudhury P (ed.). (The Electrochem. Soc., Pennington, 1992), p. 152–163.
9. Buonassisi T, Vyvenko OF, Istratov AA, Weber ER, Hahn G, Sontag D, Rakotoniaina JP, Breitenstein O, Isenberg J, Schindler R. Observation of transition metals at shunt locations in multicrystalline silicon solar cells. *Journal of Applied Physics* 2004; **95**: 1556–1561.
10. Breitenstein O, Rakotoniaina JP, Hejjo Al Rifai M, Werner M. Shunt types in crystalline silicon solar cells. *Progress in Photovoltaics: Research and Applications* 2004; **12**: 529–538.
11. Davis JR, Rohatgi A, Hopkins RH, Blais PD, Rai-Choudjury P, McCormick JR, Mollenkopf HC. Impurities in Silicon Solar Cells. *IEEE Transactions on Electronic Devices* 1980; **27**: 677–687.
12. Rand J, Rozgonyi GA, Jonczyk R, Batta S, Lu J, Reedy R, Zhang R. Characterization of Silicon-Film Sheet Material. *Proceedings of the 12th Workshop on Crystalline Silicon Solar Cell Materials and Processes*, Breckenridge, CO, 2002; 3–6.
13. Jonczyk R, Rand JA, Grenko AJ, Moyer JG. Effect of high levels of transition metals on SiliconFilm sheet silicon material. *Proceedings of the 19th European Photovoltaic Solar Energy Conference*, Paris, France, 2004. 1263–1265.
14. Plekhanov PS, Gafiteanu R, Gosele UM, Tan TY. Modeling of gettering of precipitated impurities from Si for carrier lifetime improvement in solar cell applications. *Journal of Applied Physics* 1999; **86**: 2453–2458.
15. Buonassisi T, Istratov AA, Heuer M, Marcus M, Jonczyk R, Isenberg J, Lai B, Cai Z, Heald S, Warta W, Schindler R, Willeke G, Weber ER. Synchrotron-based investigations of the nature and impact of iron contamination in multicrystalline silicon solar cell materials. *Journal of Applied Physics* 2005; **97**: 074901.
16. Buonassisi T, Marcus MA, Istratov AA, Heuer M, Ciszek TF, Lai B, Cai Z, Weber ER. Analysis of copper-rich precipitates in silicon: chemical state, gettering, and impact on multicrystalline silicon solar cell material. *Journal of Applied Physics* 2005; **97**: 063503.
17. McHugo SA, Thompson AC, Mohammed A, Lamble G, Périchaud I, Martinuzzi S, Werner M, Rinio M, Koch W, Höfs H-U, Häßler C. Nanometer-scale metal precipitates in multicrystalline silicon solar cells. *Journal of Applied Physics* 2001; **89**: 4282–4288.
18. Pizzini S, Bigoni L, Beghi M, Chemelli C. On the effect of impurities on the photovoltaic behavior of solar grade silicon. II. Influence of titanium, vanadium, chromium, iron, and zirconium on photovoltaic behavior of polycrystalline solar cells. *Journal of the Electrochemical Society* 1986; **133**: 2363–2373.
19. Ihlal A, Rizk R, Hardouin Duparc OBM. Correlation between the gettering efficiencies and the energies of interfaces in silicon bicrystals. *Journal of Applied Physics* 1996; **80**: 2665–2670.
20. Chen J, Sekiguchi T, Yang D, Yin F, Kido K, Tsurekawa S. Electron-beam-induced current study of grain boundaries in multicrystalline silicon. *Journal of Applied Physics* 2004; **96**: 5490–5495.
21. Chen J, Yang D, Zhenqiang X, Sekiguchi T. Recombination activity of Sigma 3 boundaries in boron-doped multicrystalline silicon: influence of iron recombination. *Journal of Applied Physics* 2005; **97**: 033701.
22. Ravishankar PS, Dismukes JP, Wilcox WR. Influence of ACRT on interface stability and particle trapping behavior in directional solidification of silicon. *Journal of Crystal Growth* 1985; **71**: 579–586.
23. Kalejs JP, Bathey B, Dubé C. Segregation and impurity effect in silicon growth from the melt in the presence of second phase formation. *Journal of Crystal Growth* 1991; **109**: 174–180.

24. Schönecker A, Geerligs LJ, Müller A. Casting technologies for solar silicon wafers: block casting and ribbon-growth-on-substrate. *Solid State Phenomena* 2003; **95–96**: 149–158.
25. Hall RB, Barnett AM, Collins SR, Checchi JC, Ford DH, Kendall CL, Rand J, Moore CB, in *US Patent Office, Patent Number 6,111,191* (AstroPower Inc., USA, 2000).
26. Kalejs JP. Silicon Ribbons for Solar Cells. *Solid State Phenomena* 2004; **95–96**: 159–174.
27. Hahn G, Schönecker A. New crystalline silicon ribbon materials for photovoltaics. *Journal of Physics: Condensed Matter* 2004; **16**: R1615–R1648.
28. Ciszek TF, Wang TH. Silicon defect and impurity studies using float-zone crystal growth as a tool. *Journal of Crystal Growth* 2002; **237–239**: 1685–1691.
29. Ciszek TF. In *Crystal Growth Technology*, Scheel HJ, Fukuda T (eds). John Wiley and Sons, Ltd.: Sussex, U.K., 2003; 267–289.
30. Report IEA-PVPS T1-12:2003, International Energy Agency Photovoltaic Power Systems Programme, 'Trends in Photovoltaic Applications—Survey report of selected IEA countries between 1992 and 2002,' (2003).
31. Geerligs LJ. Characterization of multi-crystalline blocks and efforts to relate their properties to the efficiencies of solar cells. *Proceedings of the 14th Workshop on Crystalline Silicon Solar Cells & Modules: Materials and Processes*, Winter Park, CO, 2004; 143–151.
32. Sinton RA, Mankad T, Bowden S, Enjalbert N. Evaluating silicon blocks and ingots with quasi-steady-state lifetime measurements. *Proceedings of the 19th European Photovoltaic Solar Energy Conference*, Paris, France, 2004; 520–523.
33. Ciszek TF. Techniques for the crystal growth of silicon ingots and ribbons. *Journal of Crystal Growth* 1984; **66**: 655–672.
34. Hanoka JI. An overview of silicon ribbon growth technology. *Solar Energy Materials & Solar Cells* 2001; **65**: 231–237.
35. Hahn G, Sontag D, Häßler C. Current collecting channels in RGS silicon solar cells—are they useful? *Solar Energy Materials & Solar Cells* 2002; **72**: 453–464.
36. Rozgonyi GA, Lu J, Zhang R, Rand J, Jonczyk R. Evaluation of silicon sheet film growth and wafer processing via structural, chemical, and electrical diagnostics. *Solid State Phenomena* 2004; **95–96**: 211–216.
37. Rand J, Rozgonyi GA, Lu J, Reedy R. Characterization of silicon-film sheet material. *Proceedings of the 29th IEEE Photovoltaic Specialists Conference*, New Orleans, USA, 2002; 98–101.
38. Buonassisi T, Istratov AA, Marcus MA, Heuer M, Pickett MD, Lai B, Cai Z, Heald SM, Weber ER. Local measurements of diffusion length and chemical character of metal clusters in multicrystalline silicon. *Solid State Phenomena* 2005; **108–109**: 577.
39. McHugo SA, Thompson AC, Flink C, Weber ER, Lamble G, Gunion B, MacDowell A, Celestre R, Padmore HA, Hussain Z. Synchrotron-based impurity mapping. *Journal of Crystal Growth* 2000; **210**: 395–400.
40. Vyvenko OF, Buonassisi T, Istratov AA, Weber ER. X-ray beam induced current/microprobe x-ray fluorescence: synchrotron radiation based x-ray microprobe techniques for analysis of the recombination activity and chemical nature of metal impurities in silicon. *Journal of Physics: Condensed Matter* 2004; **16**: S141–S151.
41. Vyvenko OF, Buonassisi T, Istratov AA, Hieslmair H, Thompson AC, Schindler R, Weber ER. X-ray beam induced current: a synchrotron radiation based technique for the in-situ analysis of recombination properties and chemical nature of metal clusters in silicon. *Journal of Applied Physics* 2002; **91**: 3614–3617.
42. Buonassisi T, Istratov AA, Pickett MD, Marcus MA, Hahn G, Riepe S, Isenberg J, Warta W, Willeke G, Ciszek T, Weber ER. Quantifying the recombination activity of metal precipitates in multicrystalline silicon using synchrotron-based spectrally-resolved X-ray beam induced current. *Applied Physics Letters* 2005; **87**: 044101.
43. Cai Z, Lai B, Yun W, McNulty I, Khounsary A, Maser J, Ilinski P, Legnini D, Trakhtenberg E, Xu S, Tieman B, Wiemerslage G, Gluskin E. Performance of a high-resolution X-ray microprobe at the Advanced Photon Source. *AIP Conference Proceeedings* 2000; **521**: 31–34.
44. Yun W, Lai B, Cai Z, Maser J, Legini D, Gluskin E, Chen Z, Krasnoperova A, Valdimirsky Y, Cerrina F, Fabrizio ED, Gentili M. Nanometer focusing of hard X-rays by phase zone plates. *Review of Scientific Instruments* 1999; **70**: 2238–2241.
45. Heald SM, Stern EA, Brewe D, Gordon RA, Crozier ED, Jiang D, Cross JO. XAFS at the Pacific Northwest Consortium-Collaborative Access Team Undulator Beamline. *Journal of Synchrotron Radiation* 2001; **8**: 342–344.
46. Underwood JH, Thompson AC, Wu Y, Giauque RD, Jones KW, Rivers ML. Elemental measurements with an X-ray microprobe of biological and geological samples with femtogram sensitivity. *Nuclear Instruments and Methods in Physics Research Section A: Accelerators, Spectrometers, Detectors and Associated Equipment* 1988; **266**: 318–323.
47. Marcus MA, MacDowell AA, Celestre R, Domning E, Franck K, Manceau A, Morrison G, Miller T, Padmore HA, Sublett RE. Beamline 10·3·2 at ALS: a hard X-ray microscope for environmental and materials sciences. *Journal of Synchrotron Radiation* 2004; **11**: 239–247.

48. Fell TS, Wilshaw PR. The effect of different transition metals on the recombination efficiency of dislocations. *Journal de Physique IV* 1991; **1**: C6–211–216.
49. Kittler M, Ulhaq-Bouillet C, Higgs V. Influence of copper contamination on recombination activity of misfit dislocations in SiGe/Si epilayers: temperature dependence of activity as a marker characterizing the contamination level. *Journal of Applied Physics* 1995; **78**: 4573–4583.
50. Lee DM, Rozgonyi GA. Low-temperature gettering of trace iron and copper by misfit dislocations in Si/Si(Ge) epitaxy. *Applied Physics Letters* 1994; **65**: 350–352.
51. McHugo SA, Thompson AC, Lamble G, Flink C, Weber ER. Metal impurity precipitates in silicon: chemical state and stability. *Physica B* 1999; **273–274**: 371–374.
52. Kazmerski LL, Ireland PJ, Ciszek TF. Evidence for the segregation of impurities to grain boundaries in multigrained silicon using Auger electron spectroscopy and secondary ion mass spectroscopy. *Applied Physics Letters* 1980; **36**: 323–325.
53. McHugo SA, Weber ER, Myers SM, Petersen GA. Competitive gettering of copper in Czochralski silicon by implantation-induced cavities and internal gettering sites. *Applied Physics Letters* 1996; **69**: 3060–3062.
54. Abrosimov NV, Bazhenov AV, Tatarchenko VA. Growth features and local electronic properties of shaped silicon. *Journal of Crystal Growth* 1987; **82**: 203–208.
55. Seager CH. Grain boundaries in polycrystalline silicon. *Annual Review of Materials Science* 1985; **15**: 271–302.
56. Istratov AA, Buonassisi T, Huber W, Weber ER. Evidence for segregation of iron at grain boundaries in polycrystalline and multicrystalline silicon. *Proceedings of the 14th NREL Workshop on Crystalline Silicon Solar Cell Materials and Processes*, Winter Park, CO, USA, 2004; 230–233.
57. Dorward RC, Kirkaldy JS. Effect of grain-boundaries on the solubility of copper in silicon. *Journal of Materials Science* 1968; **3**: 502–506.
58. Uhlmann DR, Chalmers B, Jackson KA. Interaction between particles at a solid-liquid interface. *Journal of Applied Physics* 1964; **35**: 2986–2993.
59. Rohatgi A, Davis JC, Hopkins RH, Rai-Choudhury P, McMullin PG. Effect of titanium, copper and iron on silicon solar cells. *Solid State Electronics* 1980; **23**: 415–422.
60. Graff K. *Metal Impurities in Silicon-Device Fabrication*. Springer, Berlin; New York, 2000.
61. McHugo SA, Thompson AC, Périchaud I, Martinuzzi S. Direct correlation of transition metal impurities and minority carrier recombination in multicrystalline silicon. *Applied Physics Letters* 1998; **72**: 3482–3484.
62. Buonassisi T, Istratov AA, Pickett MD, Rakotoniaina JP, Breitenstein O, Marcus MA, Heald SM, Weber ER. Transition metals in photovoltaic-grade ingot-cast multicrystalline silicon: assessing the role of impurities in silicon nitride crucible lining material. *Journal of Crystal Growth* (in press).
63. Pavarajarn V, Kimura S. Catalytic effects of metals on direct nitridation of silicon. *Journal of American Ceramic Society* 2001; **84**: 1669–1674.
64. Park D-S, Lee S-Y, Kim H-D. Extra-large grains of the silicon nitride ceramics doped with yttria and hafnia. *Journal of American Ceramic Society* 1998; **81**: 1876–1880.
65. Binetti S, Acciarri M, Savigni C, Brianza A, Pizzini S, Musinu A. Effect of nitrogen contamination by crucible encapsulation on polycrystalline silicon material quality. *Materials Science & Engineering B* 1996; **36**: 68–72.
66. Ballif C, Peters S, Borchert C, Hässler C, Isenberg J, Schindler R, Warta W, Willeke G. Lifetime investigations of deteriorated effects in processed multicrystalline silicon wafers. *Proceedings of the 17th European Photovoltaics Specialists Conference and Exhibition*, Munich, Germany, 2001; 1818–1821.
67. Rinio M, Ballif C, Buonassisi T, Borchert D. Defects in the deteriorated border layer of block-cast multicrystalline silicon ingots. *Proceedings of the 19th European Photovoltaic Solar Energy Conference and Exhibition*, Paris, France, 2004; 762–765.
68. Tsai CT. On the finite element modeling of dislocation dynamics during semiconductor crystal growth. *Journal of Crystal Growth* 1991; **113**: 499–507.
69. Franke D, Rettelbacha T, Häßler C, Koch W, Müller A. Silicon ingot casting: process development by numerical simulations. *Solar Energy Materials & Solar Cells* 2002; **72**: 83–92.
70. Steinbach I, Apel M, Rettelbach T, Franke D. Numerical simulations for silicon crystallization processes: examples from ingot and ribbon casting. *Solar Energy Materials & Solar Cells* 2002; **72**: 59–68.
71. Lu J, Wagener M, Rozgonyi G, Rand J, Jonczyk R. Effects of grain boundary on impurity gettering and oxygen precipitation in polycrystalline sheet silicon. *Journal of Applied Physics* 2003; **94**: 140–144.
72. Kalejs JP. Silicon ribbons and foils—state of the art. *Solar Energy Materials & Solar Cells* 2002; **72**: 139–153.
73. McHugo SA, Hieslmair H, Weber ER. Gettering of metallic impurities in photovoltaic silicon. *Applied Physics A: Material Science & Processing* 1997; **64**: 127–137.

74. Pizzini S. Chemistry and Physics of Segregation of Impurities at Extended Defects in Silicon. *Physica Status Solidi A* 1999; **171**: 123–132.
75. Kittler M, Seifert W. Estimation of the upper limit of the minority-carrier diffusion length in multicrystalline silicon: limitation of the action of gettering and passivation on dislocations. *Solid State Phenomena* 2004; **95–96**: 197–204.
76. Istratov AA, Buonassisi T, Marcus MA, Ciszek TF, Weber ER. Dependence of precipitation behavior of Cu and Ni in CZ and multicrystalline silicon on cooling conditions. *Proceedings of the 14th NREL Workshop on Crystalline Silicon Solar Cell Materials and Processes*, Winter Park, USA, 2004; 165–169.
77. Buonassisi T, Istratov AA, Marcus MA, Lai B, Cai Z, Heald SM, Weber ER. Engineering metal-impurity nanodefects for low-cost solar cells. *Nature Materials* 2005; **4**: 676–679.
78. Zhou T-Q, Buczkowski A, Radzimski Z, Rozgonyi GA. The gettering and electrical activity of Ni, Au, and Cu epitaxial Si/Si (2%Ge)/Si during RTA. *Proceedings of the Materials Research Society, Rapid Thermal and Integrated Processing Symposium*, Anaheim, CA, USA, 1991; 55–60.
79. Kveder V, Kittler M, Schröter W. Recombination activity of contaminated dislocations in silicon: a model describing electron-beam induced current contrast behavior. *Physical Review B* 2001; **63**: 115208.
80. Perichaud I, Martinuzzi S, Durand F. Multicrystalline silicon prepared by electromagnetic continuous pulling: recent results and comparison to directional solidification material. *Solar Energy Materials & Solar Cells* 2002; **72**: 101–107.
81. Einhaus R, Deuerinckx F, Van Kerscaver E, Szlufcik J, Durand F, Ribeyron PJ, Duby JC, Sarti D, Goaer G, Le GN, Perichaud I, Clerc L, Martinuzzi S. Hydrogen passivation of newly developed EMC-multi-crystalline silicon. *Materials Science & Engineering B* 1999; **58**: 81–85.
82. Søiland AK, Øvrelid EJ, Engh TA, Lohne O, Tuset JK, Gjerstad Ø. SiC and Si_3N_4 inclusions in multicrystalline silicon ingots. *Materials Science in Semiconductor Processing* 2004; **7**: 39–43.
83. Rakotoniaina J-P, Breitenstein O, Werner M, Al Rifai MH, Buonassisi T, Pickett MD, Ghosh M, Müller A, Nam LQ. Distribution and formation of silicon carbide and silicon nitride precipitates in block-cast multicrystalline silicon. *Proceedings of the 20th European Photovoltaic Solar Energy Conference and Exhibition*, Barcelona, Spain, 2005, 773–776.
84. Kalejs JP, Chalmers B. Melt-interface mechanism for generation of silicon carbide microdefects in silicon. *Journal of Crystal Growth* 1986; **79**: 487–492.
85. Gottschalk H. Precipitates in Ribbon Grown Solar Silicon. *Physica Status Solidi (b)* 2000; **222**: 353–365.
86. Rohatgi A. Designs and fabrication technologies for future commercial crystalline Si solar cells. *Proceedings of the 15th NREL Workshop on Crystalline Silicon Solar Cell Materials and Processes*, Vail, USA, 2005; 11–22.
87. Smith AR, McDonald RJ, Manini H, Hurley DL, Norman EB, Vella MC, Odom RW. Low-background instrumental neutron activation analysis of silicon semiconductor materials. *Journal of the Electrochemical Society* 1996; **143**: 339–346.